Title

Modeling and control of electrostatically levitated MEMS

Authors

Andonian, Michael

Pyle, Kenneth

M'Closkey, Robert

Publication Date

2021-08-11

DOI

10.1109/ccta48906.2021.9658698

Modeling and control of electrostatically levitated MEMS

Michael Andonian[1], Kenneth Pyle[2], and Robert M'Closkey[3]

***Abstract*— A system for electrostatically suspending a silicon disk between two sets of electrodes is reported. The electrodes exert electrostatic forces on the disk and also measure differential capacitances related to the disk position. There are no electrodes that directly exert in-plane forces on the disk sidewall, however, tilting the disk relative to the plane of the electrodes does exert lateral forces. Additional lateral-sensing electrodes are then used to determine the disk's lateral position so precise positioning of the disk is possible without any disk contact. Experimental stabilization results are reported.**

I. Introduction

The modeling, analysis, and control of an electrostatically suspended silicon disk is reported. The disk is a rigid six degree-of-freedom system, however, yaw motion about an axis normal to the disk is not observable with the electrode arrangement. A schematic of the disk and its electrode set is shown in Fig. 1 (the electrode-disk gaps are not to scale). Although the disk is 8.2 cm in diameter, the disk-electrode transduction gaps are only $134\,\mu$m when the disk is centered between the electrode sets. The electrostatic forces developed across such gaps are large enough to lift the disk with less than 300 V applied to the top set of electrodes. Although this is an initial proof-of-concept system, the goal is to reduce the disk size to accommodate testing of disk resonators like those described in [1].

The transduction system uses transformers in the same manner as the North American Aviation Electrostatically Levitated Gyro (ESG) [2], [3]: the electrodes measure differential capacitances related to the disk position and provide a natural null signal when the disk is centered; the same electrodes also exert controlled electrostatic forces on the disk. While this dual function of the electrodes reduces the complexity of the electronics and system design, considerable "feedthrough" is produced from the control signal to the measurements. This feedthrough must be removed from the measurements prior to implementing the controllers. One significant difference between this work and that pertaining to the ESG is the fact that stabilizing the disk is a more challenging problem than stabilizing a sphere since the latter body only requires three degrees-of-freedom to be controlled. Electrostatic suspension of spherical proof masses, albeit with different electronic schemes than those discussed in this paper, are discussed in [4], [5]. Contactless manipulation of disks is also demonstrated in [6], [7], [8] for the purpose of handling media storage. In these references, though, the disk's lateral degrees-of-freedom are not explicitly modeled and it appears that the lateral disk position is passively stabilized by fringe-field electrostatic forces which tend to center the disk under the electrodes. An electrostatically suspended ring gyro is reported in [9], however, the lateral degrees-of-freedom are controlled with electrodes that lie in the ring's plane and exert forces on the ring sidewall. The system reported herein permits the disk to undergo large, controlled lateral displacements. The electrodes do not exert strong fringe-field forces on the disk and so the lateral degrees-of-freedom are controlled by tilting the disk.

The paper is organized as follows: Sec. II describes the disk-electrode geometry; Sec. III provides details on the signal transduction scheme; Sec. IV develops and analyzes the system model; Sec. V examines controller design; Sec. VI presents the experimental results and validates the modeling paradigm; Sec. VII concludes the paper.

II. System Description

The silicon disk diameter is 8.2 cm and its thickness is $400\,\mu$m. The disk has a thin layer of sputtered aluminum to ensure it is an equipotential body. The top and bottom electrode sets are patterned on glass plates and are identical. The glass plates are not shown in Fig. 1. The glass plates are assembled so that they are parallel and an electrode on the top plate is aligned with a mirror-image electrode on the bottom plate. When the disk is uniformly centered between the electrode sets there is an electrode-disk gap of approximately $134\,\mu$m between the top of the disk and top electrode set, and a $134\,\mu$m gap between the bottom of the disk and the bottom electrode set. The four pie-shaped *primary electrodes* are labeled $\mathcal{E}_1$ through $\mathcal{E}_4$ for the top set and $\mathcal{E}_{11}$ through $\mathcal{E}_{14}$ for the bottom set. Each primary electrode has area $A_p = 10.3\,\text{cm}^2$. The primary electrodes are grouped into four pairs: the electrodes immediately facing each other (with the disk between them) form one pair, e.g., $\mathcal{E}_1$ and $\mathcal{E}_{11}$ form one primary pair. The primary pairs exert controlled electrostatic forces on the disk and also measure differential electrode-disk capacitances. The capacitance measurements are related to the electrode-disk gaps associated with each primary pair. Yaw is not observable using these measurements, nor can yaw moments be applied to the disk.

The disk's position in the X-Y plane is measured with *lateral electrodes*. In reality there are only four lateral electrodes because mirror image electrodes on the top and bottom plates actually form a single electrode as suggested

[1]Michael Andonian, PhD, is a member of the technical staff, The Aerospace Corporation, El Segundo, CA andonian23@g.ucla.edu

[2]Kenneth Pyle is a graduate student in the Mechanical and Aerospace Engineering Department, University of California, Los Angeles kennypyle@g.ucla.edu

[3]Robert M'Closkey is corresponding author and Professor in the Mechanical and Aerospace Engineering Department, University of California, Los Angeles rtm@seas.ucla.edu

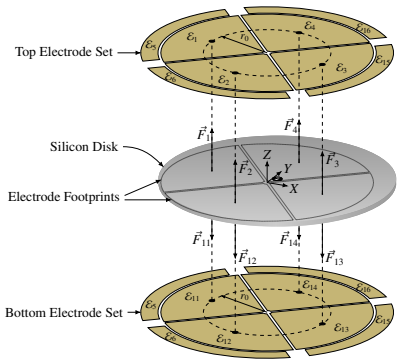

Fig. 1. Exploded view of the electrode configuration and disk. The *primary electrodes* are labeled $\mathcal{E}_1$, $\mathcal{E}_2$, $\mathcal{E}_3$ and $\mathcal{E}_4$ for the top electrode set, and $\mathcal{E}_{11}$, $\mathcal{E}_{12}$, $\mathcal{E}_{13}$ and $\mathcal{E}_{14}$ for the bottom electrode set. The *lateral electrodes* are labeled $\mathcal{E}_5$, $\mathcal{E}_{15}$, $\mathcal{E}_6$ and $\mathcal{E}_{16}$. Note that a single lateral electrode has an element on both the top and bottom. The disk center of mass is displaced from the inertial *X*-*Y*-*Z* frame in this schematic.

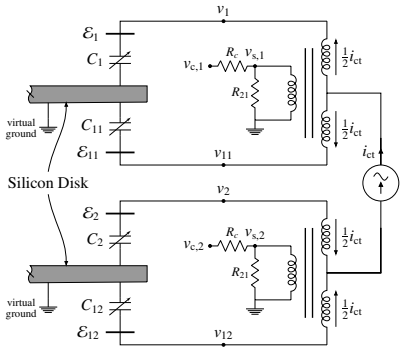

Fig. 2. Circuit schematic illustrating the connection between the transformers and the $\mathcal{E}_1$-$\mathcal{E}_{11}$ and $\mathcal{E}_2$-$\mathcal{E}_{12}$ pairs of primary electrodes. The corresponding capacitances developed between the electrodes and disk are also shown. The disk is not physically grounded, however, the notation is used to convey that the disk is at ground potential due to the coordination of the center tap currents. The connection to $\mathcal{E}_3$-$\mathcal{E}_{13}$ and $\mathcal{E}_4$-$\mathcal{E}_{14}$ is identical.

by the labels in Fig. 1. The lateral electrodes are also grouped into (two) pairs with antipodal electrodes creating a pair, e.g., $\mathcal{E}_5$ and $\mathcal{E}_{15}$ form a lateral pair, and $\mathcal{E}_6$ and $\mathcal{E}_{16}$ form the second pair. A lateral pair provides a differential capacitance measurement proportional to the lateral position of the disk relative to the pair, e.g., $\mathcal{E}_5$ and $\mathcal{E}_{15}$ measure disk displacement in the X coordinate direction. The lateral electrode configuration also largely rejects the disk's vertical and tilting rigid body motion.

The differential capacitance measurements provide convenient *null* positions: if all differential capacitances of the primary pairs are zero then the disk is parallel to the electrodes with uniform and equal gaps between the disk and primary electrodes (this assumes an ideal transformer model with no parasitic capacitance; in practice, there exist measurement offsets, but these are easily removed). Similarly, if the differential capacitances of the lateral pairs are zero then the disk is symmetrically centered relative to the lateral electrodes. Deviation from the null positions generate non-zero measurements.

The diameter spanned by the primary electrodes is smaller than the disk diameter and consequently when the disk is near its null position the net in-plane forces exerted on the disk by primary electrodes' electrical fringe fields is essentially zero. The lateral electrodes are operated at lower potentials and their fringe field forces are not modeled. It is possible to exert in-plane forces on the disk, however, this requires that the disk be tilted relative to the plane of the electrodes: the disk is an equipotential body so the field lines are normal to the disk's top and bottom surface; if the disk is tilted to be non-parallel to the primary electrodes, the electrostatic forces exerted on the disk will have a non-zero in-plane component. It will be shown how this property can be exploited to control the disk's lateral position.

III. Electrode-transformer interface

The pairing of primary electrodes is achieved with transformers as illustrated in Fig. 2. A given primary pair is connected to its transformer's primary leads. The transformer's primary windings have equal inductances connected at the center tap (ct). The center tap is driven with a sinusoidal current i_{ct}. The constant amplitude of i_{ct} is denoted a_{ct} and ω_0 is its frequency. Another transformer is connected to the center taps of two transformers linked to two primary electrode pairs. This guarantees that the total charge on the disk is constant. This is central to the operation of the system. In fact, since the disk is initially grounded, it remains at ground potential even when suspended. By maintaining the disk at ground, any difference between the capacitances in a pair of primary electrodes will produce a sinusoidal voltage drop across the transformer's secondary windings that is proportional to the imbalance. For example, the primary pairs $\mathcal{E}_k$ and $\mathcal{E}_{1k}$, $k = 1, 2, 3, 4$, are associated with capacitances C_k and C_{1k}; if $C_k = C_{1k}$ (about 77 pF when the disk is in the "null" position), indicating that the average gap between the disk and $\mathcal{E}_k$ is equal to the average gap between the disk and $\mathcal{E}_{1k}$, then $v_{\text{s},k} = 0$, where $v_{\text{s},k}$ is the "sense voltage" across the secondary winding associated with the kth set of paired electrodes. On the other hand, if the average gaps are not equal ($C_k \neq C_{1k}$) then $v_{\text{s},k}$ is sinusoidal with frequency ω_0. Synchronous demodulation of $v_{\text{s},k}$ yields a signal proportional to the imbalance in the electrode-disk gap associated with $\mathcal{E}_k$ and $\mathcal{E}_{1k}$. The phase of the demodulator is chosen to maximize the component of $v_{\text{s},k}$ due to disk displacement from its null position. The center tap current provides the master phase against which all sinusoidal signals are referenced. Furthermore, the inductances of the transformer primary windings are large enough so that the nominal inductor-capacitor resonant frequency is smaller than the carrier frequency. To first order the center tap current is evenly split between the primary inductances in a given transformer independent of the electrode-disk capacitances.

The transformers are also used for exerting controlled electrostatic forces on the disk. The sinusoidal "control" potential $v_{\text{c},k}$ is applied at resistor R_{c} that is in series with the transformer secondary load as shown in Fig. 2. The carrier frequency is also ω_0 for this signal. This produces a differential sinusoidal potential on each electrode in a primary

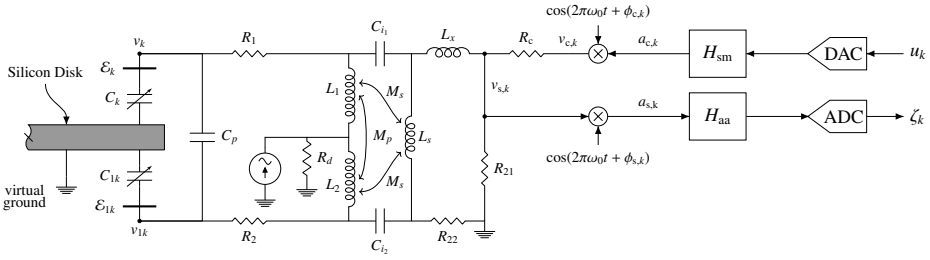

Fig. 3. Interface between the DSP and transformer signals for the primary electrodes. The anti-alias and smoothing filters are denoted H_{aa} and H_{sm}, respectively. The lateral electrodes use a similar demodulation scheme, however, since no control signals are associated with the lateral electrodes, the modulation path is not present for the lateral electrode signal conditioning.

electrode pair, i.e., electrode potentials arising from $v_{\text{c},k}$ invariably have a 180° phase difference due to the magnetic coupling within the transformer windings. In contrast, the i_{ct}-induced potentials on both electrodes are in-phase with one another. The superposed effects of i_{ct} and $v_{\text{c},k}$ create sinusoidal electrode voltages with frequency ω_0. The control signal phase $\phi_{\text{c},k}$ is selected so that changing the amplitude of $v_{\text{c},k}$, that is, changing $a_{\text{c},k}$, produces the largest *differential amplitude* change in the sinusoidal potentials on the paired electrodes. This creates the largest differential electrostatic force on the disk for a given value of $a_{\text{c},k}$. The electrostatic forces are proportional to the square of the electrode voltages so this technique exploits the fact that the disk acts as a low-pass filter: the disk responds to the mean square value of the electrode voltages.

The amplitude-modulated sinusoids $v_{\text{s},k}$ and $v_{\text{c},k}$ are related to baseband signals that are sampled and manipulated by the discrete-time controller. The modulation/demodulation shown in Fig. 3 is accomplished with analog electronics. A DSP implements the feedforward filters, coordinate transformations and the feedback compensation discussed in Sections IV and V. The "baseband" signals $\{u_1, u_2, u_3, u_4\}$ (input) and $\{\zeta_1, \zeta_2, \zeta_3, \zeta_4\}$ (output) represent an electro-mechanical model of the suspended disk.

The lateral electrodes $\mathcal{E}_5$, $\mathcal{E}_{15}$, $\mathcal{E}_6$, and $\mathcal{E}_{16}$ (see Fig. 1) measure lateral displacements of the disk and are connected to another set of transformers. This schematic is not shown given its similarity to the primary electrodes with the only difference being there is no "control" input associated with the lateral electrodes. Lateral translations of the disk change the overlapping areas between the disk and the antipodally-paired lateral electrodes (for example, $\mathcal{E}_5$ and $\mathcal{E}_{15}$ are paired via a transformer to measure the disk position in the X direction). The lateral electrodes provide the additional baseband measurements $\{\zeta_5, \zeta_6\}$, which correspond to disk displacement from it's centered null position in the X and Y coordinate directions, respectively.

IV. System Model

The transformer currents and voltages and the disk dynamics are coupled by the electrode-disk capacitances and electrostatic forces. The disk is described by generalized coordinates $q = [x, y, z, \theta, \varphi]^T$, where $\{x, y, z\}$ represent the displacement of the origin of the disk-fixed X_b-Y_b-Z_b frame from that of the inertial frame X-Y-Z. The inertial frame is situated so that X-Y are in the center-plane between the electrodes and the Z coordinate axis pierces the center of the primary electrode sets (see Fig. 1). The origin of the body-fixed frame is at the disk center of mass with X_b-Y_b in the disk plane. Successive rotations about the X-axis and Y_b-axis are given by the θ-φ Euler angle sequence. When $q = 0$ the body-fixed frame and inertial frame are coincident. This is the desired equilibrium configuration of the disk.

The disk is constrained to very small rotations and its diameter-to-thickness ratio is approximately 100. A number of simplifying assumptions can be made. First, since the disk is thin, calculation of electrode-disk gaps is determined by the deflection of the disk's center-plane and small angle approximations can be used for defining the gaps. The vertical displacement of the disk at the location of the primary electrodes' centroids are defined

$$\begin{aligned} z_1 &= z + (r_0 + x)\,\varphi - y\theta \\ z_2 &= z - (r_0 + y)\,\theta + x\varphi \\ z_3 &= z - (r_0 - x)\,\varphi - y\theta \\ z_4 &= z + (r_0 - y)\,\theta + x\varphi. \end{aligned} \tag{1}$$

where r_0 represents the radius of a circle in the electrode plane that interpolates the primary electrodes' centroids. The electrodes' centroids are where the "effective" electrostatic forces act and are also used to define the effective gap for capacitance calculations. The forces $\vec{F}_1$, $\vec{F}_{11}$, etc., in Fig. 1 are located at these centroids. Fig. 4 also clarifies the relationships by showing side views of the electrodes and disk. Thus, the $\mathcal{E}_1$-disk gap is given by $z_0 - z_1$, the $\mathcal{E}_{11}$-disk gap is given by $z_0 + z_1$, and so forth.

The disk-electrode capacitances are determined from a parallel plate model using the effective electrode-disk gaps

$$\begin{aligned} C_k\,(q) &= \frac{\epsilon_0 \epsilon_r A_{\text{p}}}{z_0 - z_k} \\ C_{1k}\,(q) &= \frac{\epsilon_0 \epsilon_r A_{\text{p}}}{z_0 + z_k} \end{aligned} \quad k = 1, 2, 3, 4 \tag{2}$$

where A_{p} represents the primary electrode area. As mentioned above, the distributed electrostatic forces are replaced by point forces acting at the centroids. The magnitude of point forces associated with the primary electrode pair $\mathcal{E}_k$ and $\mathcal{E}_{1k}$ are

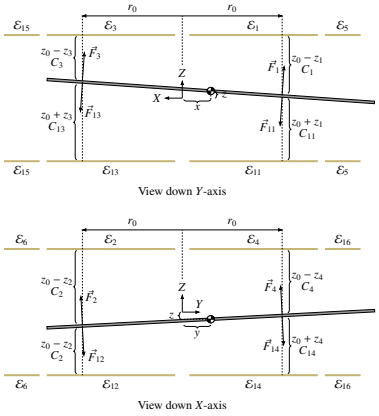

Fig. 4. Side views of the disk in relation to the electrode configuration (not to scale). The disk is assumed to be thin for the purpose of determining the locations of the electrostatic forces acting on it.

similarly computed assuming a parallel plate model,

$$F_k = \frac{\epsilon_0 \epsilon_r A_\mathrm{p}}{2(z_0 - z_k)^2} v_k^2 \qquad k = 1,2,3,4 \tag{3}$$
$$F_{1k} = \frac{\epsilon_0 \epsilon_r A_\mathrm{p}}{2(z_0 + z_k)^2} v_{1k}^2.$$

The electrostatic forces exerted on the disk by the lateral electrodes are neglected. These electrodes are significantly smaller than the primary electrodes and are operated at lower potentials.

The generalized forces associated with the generalized coordinates are computed assuming small angles. The details of these routine calculations are not given. Lagrange's method yields

$$m\ddot{x} = \varphi \sum_{k=1}^{4} (F_k - F_{1k}), \quad m\ddot{y} = -\theta \sum_{k=1}^{4} (F_k - F_{1k})$$
$$m\ddot{z} + mg = -c_z \dot{z} + \sum_{k=1}^{4} (F_k - F_{1k})$$
$$(J_{xy} \cos^2\varphi + J_z \sin^2\varphi)\ddot{\theta} + \dot{\varphi}\sin(2\varphi)(J_z - J_{xy})\dot{\theta} = Q_\theta - c_\theta \dot{\theta}$$
$$J_{xy}\ddot{\varphi} + \frac{1}{2}\sin(2\varphi)(J_{xy} - J_z)\dot{\theta}^2 = Q_\varphi - c_\varphi \dot{\varphi}$$

where Q_θ and Q_φ are the generalized moments (the expressions are not shown to conserve space). The disk mass and moments of inertia are denoted m and $\{J_z, J_{xy}\}$, respectively. Squeeze-film damping between the disk and the electrodes are represented by c_z, c_θ, and c_φ. The damping estimates are taken from [10]. It is clear from these equations that forces in the *lateral* directions are only produced when the disk angles are non-zero. This implies disk motion in the X-Y plane may be controlled by tilting the disk. Similarly, translation in the X-Y plane changes the moments applied to the disk and therefore affects the disk angles. Thus, the lateral and rotational components are intrinsically coupled.

The disk equations of motion can be represented as first-order ODEs in the form

$$\frac{d}{dt}\begin{bmatrix} q \\ \dot{q} \end{bmatrix} = \begin{bmatrix} \dot{q} \\ f(q, \dot{q}, w) \end{bmatrix} \tag{4}$$

where q is the vector of generalized coordinates, w is the vector of transformer variables defined below, and $f(q, \dot{q}, w)$ is the vector function of normalized forces and moments.

The electrical subsystem model has been extensively described elsewhere and is only briefly reviewed. Fig. 2 shows schematics to clarify how the transformers are connected to the electrodes in Fig. 1. Using the transformer models from [11], [12], the electrical subsystem equations of motion are

$$M(q)\dot{w} = Aw + B_1 i_\mathrm{ct} + B_2 v_\mathrm{c}, \quad v_\mathrm{s} = Jw, \tag{5}$$

where w denotes the vector of currents and voltages associated with the electrode pairs $\{\mathcal{E}_k, \mathcal{E}_{1k}\}$, $k = 1,2,3,4$, and the transformers, i_ct is the center tap current, and $v_\mathrm{c} = [v_{\mathrm{c},1}, v_{\mathrm{c},12}, v_{\mathrm{c},13}, v_{\mathrm{c},4}]^T$ and $v_\mathrm{s} = [v_{\mathrm{s},1}, v_{\mathrm{s},2}, \ldots, v_{\mathrm{s},6}]^T$ represent the control voltages and sense voltages associated with the transformers' secondary windings (see Fig. 3). As discussed in [11], these equations are overdetermined but convenient to use when describing the transformers. The mass matrix $M(q)$ depends on the disk coordinates q because the disk position establishes the electrode-disk capacitances.

Additional states are contributed by the analog anti-alias filters and DAC smoothing filters shown in Fig. 3. The DAC smoothing filter transfer functions are denoted H_sm. The output of the smoothing filters are the signals $a_{\mathrm{c},k}$. The $v_{\mathrm{c},k}$ signals are created by sinusoidally modulating $a_{\mathrm{c},k}$,

$$v_{\mathrm{c},k} = a_{\mathrm{c},k}\cos(2\pi\omega_0 t + \phi_{u,k}),\ k = 1,\ldots,4 \tag{6}$$

where the phases are selected to achieve the maximum change in differential amplitude of the $\{\mathcal{E}_k, \mathcal{E}_{1k}\}$ electrode potentials. The smoothing filters are identical and are collectively modeled by the continuous-time state-space matrices $(A_\mathrm{sm}, B_\mathrm{sm}, C_\mathrm{sm}, 0)$ with state vector q_sm, and output $a_\mathrm{c} = [a_{\mathrm{c},1}, a_{\mathrm{c},2}, a_{\mathrm{c},3}, a_{\mathrm{c},4}]^T$. The diagonal matrix of modulating sinusoids is defined,

$$\mathcal{D}_\mathrm{c} = \mathrm{diag}\left(\cos(2\pi\omega_0 t + \phi_{u,1}), \ldots, \cos(2\pi\omega_0 t + \phi_{u,4})\right),$$

so the sinusoidal control signals at the transformers' secondary windings are $v_\mathrm{c} = [v_{\mathrm{c},1}, v_{\mathrm{c},2}, v_{\mathrm{c},3}, v_{\mathrm{c},4}]^T = \mathcal{D}_\mathrm{c} a_\mathrm{c}$.

Demodulating and filtering $v_{\mathrm{s},k}$ removes the $2\omega_0$ harmonic components. The filtering is accomplished using identical anti-alias filters whose transfer functions are denoted H_aa. The inputs to the anti-alias filters are

$$a_{\mathrm{s},k} := v_{\mathrm{s},k}\cos(2\pi\omega_0 t + \phi_{\mathrm{s},k}), \quad k = 1,\ldots,6, \tag{7}$$

The outputs of the anti-alias filters are the baseband signals ζ_k sampled by the DSP. The anti-alias filters are gathered into a single state-space representation $(A_\mathrm{aa}, B_\mathrm{aa}, C_\mathrm{aa}, 0)$ with state vector q_aa, input $a_\mathrm{s} = [a_{\mathrm{s},1}, \ldots, a_{\mathrm{s},6}]^T$, and output $\zeta = [\zeta_1, \ldots, \zeta_6]^T$. The diagonal matrix of sinusoids that demodulate v_s is defined

$$\mathcal{D}_\mathrm{s} = \mathrm{diag}\left(\cos(2\pi\omega_0 t + \phi_{s,1}), \ldots, \cos(2\pi\omega_0 t + \phi_{s,6})\right)$$

so $a_\mathrm{s} = \mathcal{D}_\mathrm{s} v_\mathrm{s}$. Collectively, the full coupled system is governed

by

$$\begin{aligned} \dot{q}_{\rm sm} &= A_{\rm sm}q_{\rm sm} + B_{\rm sm}u_c, \quad a_{\rm c} = C_{\rm sm}q_{\rm sm} \\ M(q)\dot{w} &= Aw + B_1 i_{\rm ct} + B_2\mathcal{D}_{\rm c}a_{\rm c}, \quad v_{\rm s} = Jw \\ \dot{q}_{\rm aa} &= A_{\rm aa}q_{\rm aa} + B_{\rm aa}\mathcal{D}_{\rm s}v_{\rm s}, \quad \zeta = C_{\rm aa}q_{\rm aa} \\ \frac{d}{dt}\begin{bmatrix} q \\ \dot{q} \end{bmatrix} &= \begin{bmatrix} \dot{q} \\ f(q,\dot{q},w) \end{bmatrix}. \end{aligned} \tag{8}$$

A. Model Linearization

A periodic solution of (8) can be found with the disk at equilibrium between the electrode sets. This occurs when $q = 0$, $\dot{q} = 0$ and when the mean-value of the electrostatic forces and gravitational force sum to zero in the Z direction and also exert zero net moment on the disk. The elements of $u_{\rm c}$ are adjusted until the zero net force and zero moment conditions are achieved. The offset of u_c at this condition is denoted $\bar{u}$ so for purposes of deriving the linearization $u_{\rm c} = \bar{u} + u$, i.e. the linearization input is u. The sinusoidal steady-state response of the transformer variables, denoted w_0, is computed from (5) assuming $q = 0$, $\dot{q} = 0$ and $u_c = \bar{u}$. Linear variational equations are determined about $q = 0$, $\dot{q} = 0$ and w_0 and yield a linear time-periodic model,

$$\begin{aligned} \dot{\delta} &= A_\delta(t)\delta + B_\delta(t)u \\ \zeta &= C_\delta\delta. \end{aligned}, \tag{9}$$

where δ represents the state vector of perturbation variables. The equations are time-periodic with period $1/\omega_0$.

Analysis of (9) is carried out using the parameters reported in [11] for all of the transformers. Furthermore, the carrier frequency, center tap currents, and each element of the control voltage offset to establish an equilibrium position for the disk are $\omega_0 = 25\,\text{kHz}$, $a_{\rm ct} = 15.5\,\text{mA}$, and $\bar{u} = 1.77\,\text{V}$, respectively. The anti-alias filters and smoothing filters are 4-pole Butterworth with 1 kHz corner frequencies. This produces a system model with 86 states, i.e. $\delta \in \mathbf{R}^{86}$.

The solution to an initial value problem for (9) is,

$$\delta(t) = \Theta(t,t_0)\delta(t_0) + \int_{t_0}^{t} \Theta(t,\tau)B_\delta(\tau)u(\tau)d\tau, \tag{10}$$

$t \geq t_0$, where $\delta(t_0)$ is the initial condition represented in the perturbation variables, and $\Theta(t,t_0)$ represents the state transition matrix associated with (9). The "start time" t_0 determines the phase of the time-periodic steady-state solution about which the linearization is computed. It was shown in [11] that the choice of t_0 has no practical impact on the subsequent model, thus, it is assumed $t_0 = 0$ for the remainder of the analysis. A time-invariant discrete-time model can be derived by noting that the DSP sample period, t_s, is selected to be five times the period of the carrier, i.e. $t_s\omega_0 = 5$. Successive samples at the DSP sample rate can be related using (10)

$$\begin{aligned} \delta((k+1)t_s) &= \Theta((k+1)t_s, kt_s)\delta(kt_s) \\ &\quad + \int_{kt_s}^{(k+1)t_s} \Theta((k+1)t_s,\tau)B_\delta(\tau)u(\tau)d\tau, \end{aligned} \tag{11}$$

where k is the integer sample index. Because of the zero-order hold implemented by the DAC, $u(\tau)$ can be replaced by $u(kt_s)$ in the integral. Thus, the time-invariant discrete-time model from the perspective of the DSP that implements the controllers is

$$\begin{aligned} \delta[k+1] &= \Phi\delta[k] + \Gamma u[k] \\ \zeta[k] &= C_\delta\delta[k], \end{aligned} \tag{12}$$

where

$$\Phi := \Theta(t_s,0), \quad \Gamma := \int_0^{t_s} \Theta(t_s,\tau)B_\delta(\tau)d\tau. \tag{13}$$

and where the notation $\delta[k]$ has replaced $\delta(kt_s)$ and so forth.

This analysis yields the four-input/six-output system denoted P. The frequency response of (12) is shown in Fig. 5. A notable feature of the model is presence of *three* unstable eigenvalues with continuous-time values equal to 6.4 rad/s and 7.0 rad/s, the latter eigenvalue having algebraic and geometric multiplicity two. It will be shown that these eigenvalues can be associated with disk's vertical translation (6.4 rad/s) and its two "tilt" degrees of freedom (the repeated eigenvalue 7.0 rad/s). There are also two pairs of stable lightly-damped eigenvalues that correspond to two resonant modes with natural frequencies near 0.2 Hz. Due to the symmetry of the disk and identical transformer models, a permutation of indices will produce the plant response to the other inputs, e.g., $\zeta_2/u_2 = \zeta_1/u_1$. Also of interest is the presence of "feedthrough" coupling in ζ_1/u_1 and the other "diagonal" channels. This coupling is caused by using each primary electrode for actuation and sensing (see the relation of $v_{s,k}$ and $v_{c,k}$ in Fig. 3). The coupling must be reduced to practically stabilize the disk and in practice a MIMO FIR filter is identified from measurements and is used as a feedforward filter.

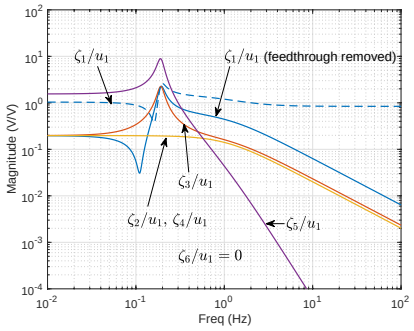

Fig. 5. Frequency response of P associated with input u_1. The ζ_1 output is shown with and without the feedthrough. The feedthrough in the ζ_k/u_l, $k \neq l$, channels is negligible.

V. Controller design

A loop shaping design technique based on decoupling transformations is used to stabilize the system. Additional synthesis approaches will be addressed in future papers. The new input-output variables are more directly related to the disk's rigid body motion. The new input and output variables are defined $\{u_z, u_\varphi, u_\theta\}$ and $\{v_z, v_\varphi, v_\theta, v_x, v_y\}$, respectively, and are related to the original input-output variables according to

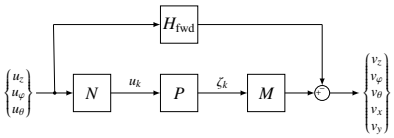

Fig. 6. The feedforward-compensated and decoupled plant $\tilde{P} = MPN - H_{\text{fwd}}$. The feedforward filter is denoted H_{fwd}.

Fig. 6 where the matrices M and N are defined,

$$M = \begin{bmatrix} 0.5 & 0.5 & 0.5 & 0.5 & 0 & 0 \\ \frac{1}{\sqrt{2}} & 0 & -\frac{1}{\sqrt{2}} & 0 & 0 & 0 \\ 0 & -\frac{1}{\sqrt{2}} & 0 & \frac{1}{\sqrt{2}} & 0 & 0 \\ 0 & 0 & 0 & 0 & 1 & 0 \\ 0 & 0 & 0 & 0 & 0 & 1 \end{bmatrix}, N = \begin{bmatrix} 0.5 & \frac{1}{\sqrt{2}} & 0 \\ 0.5 & 0 & -\frac{1}{\sqrt{2}} \\ 0.5 & -\frac{1}{\sqrt{2}} & 0 \\ 0.5 & 0 & \frac{1}{\sqrt{2}} \end{bmatrix}.$$

The new output variable v_z can be interpreted as the average gap between the disk and electrodes. Similarly, since v_φ is proportional to the difference between ζ_1 and ζ_3, it is related to an angle. From the input perspective, a moment is applied about the X coordinate axis when $u_\theta \neq 0$, and, similarly, a moment is applied about the Y coordinate axis when $u_\varphi \neq 0$. A vertical electrostatic force is applied to the disk with u_z. Feedthrough compensation can be performed using the original input-output variables, however, it is more convenient to remove the feedthrough after the input-output transformations as illustrated in Fig. 6. This approach is adopted in the experiments.

The system $\tilde{P} = MPN - H_{\text{fwd}}$ is used for controller design. It is referred to as the "decoupled" plant because the transfer function has only non-zero entries in the $(1,1)$, $(2,2)$, $(3,3)$, $(4,2)$ and $(5,3)$ elements. Note that the $(1,1)$ element is referred to as v_z/u_z, the $(2,2)$ element as v_φ/u_φ, and so forth. The frequency response magnitudes of the non-zero elements of $\tilde{P}$ are shown in Fig. 7. Also shown are the perturbation variables $\{\delta_z, \delta_\varphi, \delta_\theta, \delta_x, \delta_y\}$ associated with the disk's kinematic variables. The perturbation variables are not directly assessable in the physical system, however, they can be extracted from the model and compared to the electrical measurements $\{v_z, v_\varphi, v_\theta, v_x, v_z\}$. It is evident from Fig. 7 that the electrical measurements are excellent proxies for the disk's kinematic variables. This justifies the choice of subscript for the electrical measurements. The *scale factors* associated with the electrical measurements can be extracted from these graphs by comparing the magnitude of v_z/u_z to that of δ_z/u_z and so on. The scale factors are estimated to be: 1.03 mrad/V for θ and φ; 16.5 μm/V for z; 2.87 mm/V for x and y.

The controller topology is shown in Fig. 8. The SISO controllers, denoted G_z, G_φ and G_θ, are separately designed for v_z/u_z, v_φ/u_φ, and v_θ/u_θ. These controllers stabilize the closed-loop system. The disk's lateral position is regulated by using the lateral position error as the *references* (r_φ, r_θ) for the tilt degrees-of-freedom controllers. Thus, the lateral position of the disk is controlled by tilting the disk.

The v_z/u_z transfer function has only one unstable pole at 6.4 rad/s –this pole is referred to as the "z-instability" of the disk. The magnitude of v_z/u_z exhibits a low-pass characteristic whose corner frequency corresponds to this

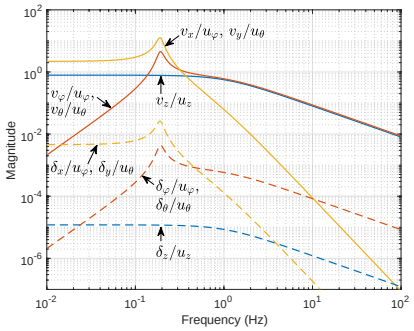

Fig. 7. Frequency response of $\tilde{P}$ compared to the frequency response of the disk's kinematic perturbation variables $\{\delta_z, \delta_\varphi, \delta_\theta, \delta_x, \delta_y\}$.

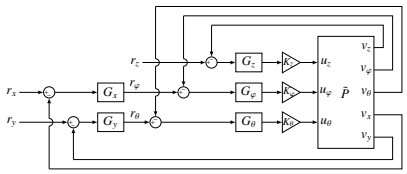

Fig. 8. Closed-loop block diagram.

unstable pole. It is a simple matter to stabilize the z-instability using constant gain feedback, however, due to uncertainty in the feedthrough cancellation at higher frequencies in the actual system, the controller gain is rolled off after 100 Hz. Thus, the (continuous-time) transfer function of the z-DOF controller, denoted G_z, is

$$G_z = 4\frac{200\pi}{s + 200\pi}. \tag{14}$$

The loop gain Nyquist plots are shown in Fig. 9.

The tilt transfer function v_φ/u_φ only has one unstable pole at 7.0 rad/s. This pole is referred to as a "tilt-instability." A companion tilt-instability appears in v_θ/u_θ. Thus, the tilt instabilities associated with the double eigenvalue at 7.0 rad/s are present in v_φ/u_φ and v_θ/u_θ, but only as a single unstable pole in each of these transfer functions. Other notable features of the tilt transfer functions are the double zeros at the origin. This creates the ω^2 trend at low frequencies in Fig. 7 and implies that the disk angles must be zero when the disk is at equilibrium.

Stabilizing the tilt degrees of freedom is an interesting problem because v_φ/u_φ (and, hence, v_θ/u_θ) is not *strongly stabilizable*. This can be illustrated by analyzing the parity interlacing property of the poles and zeros and also by analysis of the Nyquist plot. The following controller is implemented for v_φ/u_φ,

$$G_\varphi = \frac{14\pi}{s + 14\pi} \frac{s^2 + 0.2\omega_n s + \omega_n^2}{s^2 + 2\omega_n s + \omega_n^2} \frac{s + 3}{s - 3}, \quad \omega_n = 0.4\pi, \tag{15}$$

where the unstable pole is located at 3 rad/s. The Nyquist plot of loop gain is shown in Fig. 9. An identical controller is used to stabilize the unstable pole in v_θ/u_θ associated with the second tilt-instability ($G_\theta = G_\varphi$).

Analysis of the plant model with the controllers (14) and (15) demonstrates that the closed-loop system is asymptotically stable. Further analysis reveals that the lateral

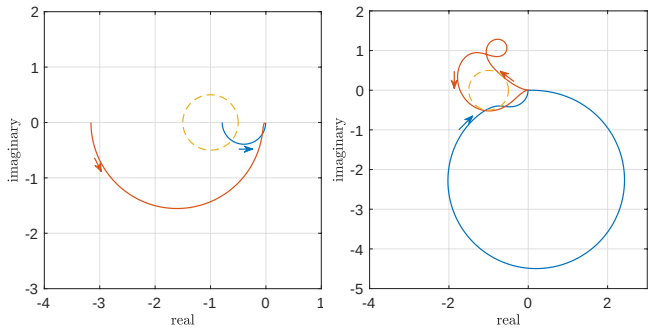

Fig. 9. **Left:** Nyquist plot of v_z/u_z (blue) and the loop gain (red) illustrating one counterclockwise encirclement of -1. **Right:** Nyquist plot of v_φ/u_φ (blue) and the loop gain indicating two counterclockwise encirclements of -1 (red). The arrows indicate the direction of increasing frequency for $\omega \geq 0$.

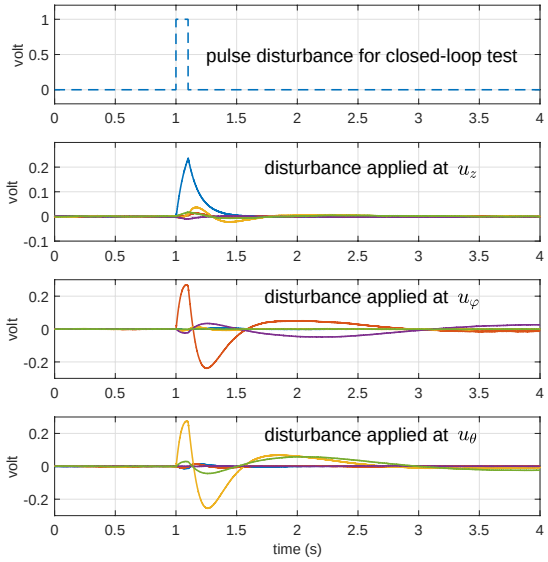

Fig. 10. Closed-loop experiments showing response to a pulse disturbance (shown dash blue) applied at the inputs of $\tilde{P}$. The disk is suspended without contact. Blue solid is v_z; red is v_φ; yellow is v_θ; purple is v_x; green is v_y.

controllers can be selected as simple gains in order to regulate the disk's lateral position,

$$G_x = 1, \quad G_y = -1. \tag{16}$$

VI. Experimental results

The controllers are discretized and implemented as given in (14)–(16). Only minor adjustments to the gains $\{K_z, K_\varphi, K_\theta\}$ are performed. The disk is demonstrated to be stably suspended by introducing pulse disturbances into the closed-loop system at the input of $\tilde{P}$. The pulse is sequentially summed in with the controller outputs in order to perturb u_z, u_φ and u_θ. The results of this experiment are shown in Fig. 10. The disk returns to its equilibrium position (0 V represents the equilibrium configuration of the disk because measurement offsets have been removed).

The physical plant exhibits cross-channel coupling that does not exist in the model, however, this is not surprising because small differences in the transduction gains associated with the primary electrode pairs and their transformers will destroy the symmetry in the model so that the decoupling transformations M and N actually mix all of the measurements related to the disk's kinematic variables.

The scale factors that have been estimated from the model have not been independently verified, however, vibrometer measurements of the beam system described in [11], which uses a transduction scheme that is identical to the present work, shows that the model-based scale factor deviates less than 10% from the measurement-based scale factor so similar accuracy is expected in this work.

VII. Conclusion

Electrostatic suspension of an untethered and contact-free platform –a thin silicon disk– has been demonstrated, however, there are host of interesting system and controls issues that can be addressed including: efficient testing and identification techniques to extract (unstable) models from test data; systematic uncertainty modeling and robust controller synthesis for improving the stability margins; synthesizing stable controllers (the plant has no real, unstable blocking zeros so there are no structural impediments to accomplishing this). There are also a number of issues associated with the design of the system including: signal processing techniques to eliminate the feedthrough coupling and therefore obviate the need for the feedforward filters; design of the electrode layout for improved control authority. These topics will be addressed in future papers.

Acknowledgement: The authors thank the staff of the UCLA Nanoelectronics Research Facility. This research did not receive any specific grant from funding agencies in the public, commercial, or not-for-profit sectors.

References

[1] A. H. Behbahani, D. Kim, P. Stupar, J. DeNatale, and R. T. M'Closkey, "Tailored etch profiles for wafer-level frequency tuning of axisymmetric resonators," *J. Microelectromech. Syst.*, vol. 26, no. 2, pp. 333–343, April 2017.

[2] J. L. Atkinson, "Electrostatic bearing," U.S. Patent 3 334 949, 1967.

[3] ——, "Electrostatic bearing sensing and control circuitry," U.S. Patent 3 891 285, 1975.

[4] R. Toda, N. Takeda, T. Murakoshi, S. Nakamura, and M. Esashi, "Electrostatically levitated spherical 3-axis accelerometer," in *Proc. Fifteenth IEEE Intl. Conf. Microelectromech. Sys. (MEMS 2002)*, Jan 2002, pp. 710–713.

[5] F. Han, Z. Gao, D. Li, and Y. Wang, "Nonlinear compensation of active electrostatic bearings supporting a spherical rotor," *Sens. Actuator A Phys.*, vol. 119, no. 1, pp. 177–186, 2005.

[6] J. Jin, T. Higuchi, and M. Kanemoto, "Electrostatic levitator for hard disk media," *IEEE Trans. Ind. Electron.*, vol. 42, no. 5, pp. 467–473, 1995.

[7] J. U. Jeon and T. Higuchi, "Electrostatic suspension of dielectrics," *IEEE Trans. Ind. Electron.*, vol. 45, no. 6, pp. 938–946, 1998.

[8] E. van West, A. Yamamoto, and T. Higuchi, "Manipulation of thin objects using levitation techniques, tilt control, and haptics," *IEEE Trans. Automat. Sci. Eng.*, vol. 7, no. 3, pp. 451–462, 2010.

[9] T. Murakoshi, Y. Endo, K. Fukatsu, S. Nakamura, and M. Esashi, "Electrostatically levitated ring-shaped rotational-gyro/accelerometer," *Jpn. J. Appl. Phys.*, vol. 42, no. 4B, pp. 2468–2472, Apr. 2003.

[10] M. Bao and H. Yang, "Squeeze film air damping in MEMS," *Sens. Actuator A Phys.*, vol. 136, no. 1, pp. 3 – 27, 2007.

[11] M. Andonian and R. T. M'Closkey, "Sensing and control interface for precise gap control," *Mechatronics*, vol. 56, pp. 277 – 286, 2018.

[12] ——, "Identification and compensation of feedthrough in an unstable electrostatic bearing," *Mechatronics*, vol. 65, p. 102315, 2020.